molecules

MDPI

Article

Synthesis of a Chiral 3,6T22-Zn-MOF with a T-Shaped Bifunctional Pyrazole-Isophthalate Ligand Following the Principles of the Supramolecular Building Layer Approach

Dennis Woschko, Simon Millan, Muhammed-Ali Ceyran, Robert Oestreich and Christoph Janiak *

Institut für Anorganische Chemie und Strukturchemie, Heinrich-Heine-Universität Düsseldorf, 40225 Düsseldorf, Germany

* Correspondence: janiak@uni-duesseldorf.de; Tel.: +49-211-81-12286

Abstract: The metal–organic framework (MOF) [Zn(Isa-az-tmpz)]·~1–1.5 DMF with the novel T-shaped bifunctional linker 5-(2-(1,3,5-trimethyl-1H-pyrazol-4-yl)azo)isophthalate (Isa-az-tmpz) was obtained as a conglomerate of crystals with varying degrees of enantiomeric excess in the chiral tetragonal space groups $P4_32_12$ or $P4_12_12$. A topological analysis of the compound resulted in the rare **3,6T22**-topology, deviating from the expected **rtl**-topology, which has been found before in pyrazolate-isophthalate-functionalized MOFs using the supramolecular building layer (SBL) approach. **3,6T22**-[Zn(Isa-az-tmpz)]·~1–1.5 DMF is a potentially porous, three-dimensional structure with DMF molecules included in the corrugated channels along the *a* and *b*-axis of the as synthesized material. The small trigonal cross-section of about 6 × 4 Å (considering the van der Waals surface) prevents the access of N_2 and Ar under cryogenic conditions. After activation, only smaller H_2 (at 87 K) and CO_2 (at 195 K) are allowed for gas uptakes of 2 mmol g^{-1} and 5.4 mmol g^{-1}, respectively, in the ultramicroporous material, for which a BET surface area of 496 $m^2 \cdot g^{-1}$ was calculated from CO_2 adsorption. Thermogravimetric analysis of the compound shows a thermal stability of up to 400 °C.

Keywords: metal-organic frameworks (MOF); zinc; topologies; T-shaped linker; bifunctional pyrazole-carboxylate linker; conglomerate; enantiomeric excess; chiral space group

Citation: Woschko, D.; Millan, S.; Ceyran, M.-A.; Oestreich, R.; Janiak, C. Synthesis of a Chiral 3,6T22-Zn-MOF with a T-Shaped Bifunctional Pyrazole-Isophthalate Ligand Following the Principles of the Supramolecular Building Layer Approach. *Molecules* **2022**, *27*, 5374. https://doi.org/10.3390/molecules27175374

Academic Editors: Marina Fonari and Rodica Olar

Received: 22 July 2022
Accepted: 17 August 2022
Published: 23 August 2022

1. Introduction

Metal–organic frameworks (MOFs) are a much-studied topic with a wide variety of potential applications, interesting properties and topologies [1–3]. There are many factors that can influence the synthesis, growth and the structure of MOFs. One approach to designing MOFs with a certain structure and underlying net is the 'supramolecular building layer approach', formulated by Guillerm et al. [4]. Within this approach, multiple ways were rationalized to obtain MOFs with certain topologies through the inter-connection of two-dimensional nets with accessible perpendicular bridging sites. One of the best-known strategies is the use of 4,4′-bipyridine derivates to connect carboxylate-based paddlewheel clusters along the axial open metal sites, thereby effectively turning the tetragonal 4-c (four-connected) nodes into octahedral 6-c-nodes [5–8]. Seki et al. were among the first to utilize this strategy using copper (II) terephthalate and triethylenediamine as a pillaring ligand to synthesize a mixed-ligand MOF with a **pcu** topology [9]. The success of this strategy led to the synthesis and use of new bifunctional ligands, wherein the dicarboxylate group constructs a two-dimensional net while a N-heterocycle functions as an axial pillaring unit, unifying the mixed-ligand approach. This strategy has been termed 'ligand-to-axial pillaring' by Eubank et al. based on the utilization of T-shaped bifunctional ligands that function as a 3-c node [4,10]. Using this strategy, a plethora of 3,6-c connected MOFs, with topologies such as **apo** (α-PO2), [10] **eea** (based on the Kagomé-lattice (**kgm**)) [10–12], **pyr** (pyrite) [12] and **rtl** (rutile) [10,12–14], have been synthesized.

Among the utilized bifunctional T-shaped ligands to synthesize these 3,6-c connected MOFs the pyrazole-carboxylate ligands have some especially interesting properties compared to the more commonly used pyridine–carboxylate ligands, since they have an additional NH-function, which can act as an additional interaction site [13,15]. 5-(Pyrazole-4-yl)isophthalic acid (H_3Isa-pz) (Scheme 1), as the simplest T-shaped pyrazole-carboxylate ligand, has been used by Ma et al. to synthesize **rht**-MOF-pyr. This MOF consists of a copper paddlewheel unit connected through the isophthalate oxygen atoms and a trinuclear copper cluster connected through both pyrazole nitrogen atoms [16]. The azo-functionalized T-shaped ligand 5-(4-(3,5-dimethyl-1H-pyrazolyl)azo)isophthalic acid (H_3Isa-az-dmpz) (Scheme 1) has been utilized by Millan et al. to obtain two **rtl**-MOFs with copper and zinc [13]. The copper MOF **rtl**-[Cu(HIsa-az-dmpz)] showed a good CO_2 uptake while the zinc MOF **rtl**-[Zn(HIsa-az-dmpz)] went through an irreversible transformation into a non-porous compound [13]. The azo group in the linkers H_3Isa-az-dmpz and H_2Isa-az-tmpz could be used for trans-cis photoisomerization effects in future studies [17–19].

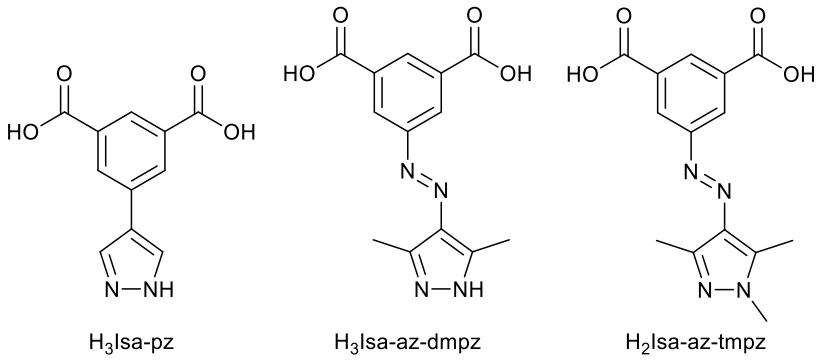

Scheme 1. The literature reported T-shaped bifunctional pyrazole-isophthalic acid ligands 5-(pyrazole-4-yl)isophthalic acid (H_3Isa-pz) [16], 5-(4-(3,5-dimethyl-1H-pyrazolyl)azo)isophthalic acid (H_3Isa-az-dmpz) [13] and 5-(2-(1,3,5-trimethyl-1H-pyrazol-4-yl)azo)isophthalic acid (H_2Isa-az-tmpz) used in this work.

Herein, we present the successful synthesis of a new 3,6-c connected MOF [Zn(Isa-az-tmpz)], following the ligand-to-axial pillaring approach. Instead of the expected **rtl**-topology, which had been found for the MOFs **rtl**-[Cu(HIsa-az-dmpz)] and **rtl**-[Zn(HIsa-az-dmpz)] with the related HIsa-az-dmpz^{2-} linker [13], here, the rare chiral **3,6T22**-topology was obtained in [Zn(Isa-az-tmpz)]·~1–1.5 DMF through the reaction of $Zn(NO_3)_2 \cdot 4\ H_2O$ with the newly synthesized T-shaped pyrazole-carboxylate ligand Isa-az-tmpz^{2-} (5-(2-(1,3,5-trimethyl-1H-pyrazol-4-yl)azo)isophthalate). Chiral MOFs are of interest for chiral separation and catalysis [20–22].

2. Results and Discussion

The compound [Zn(Isa-az-tmpz)]·~1–1.5 DMF was obtained through the reaction of $Zn(NO_3)_2 \cdot 4\ H_2O$ with 5-(2-(1,3,5-trimethyl-1H-pyrazol-4-yl)azo)isophthalic acid (H_2Isa-az-tmpz) in DMF at 80 °C. This synthesis yielded yellow octahedral-shaped crystals of formula [Zn(Isa-az-tmpz)]·~1–1.5 DMF. The comparison between the morphology of the single crystal used for the measurement and the theoretical morphology calculated with MERCURY from the crystal structure showed a decent match (Figure 1) [23].

The asymmetric unit consisted of one Zn(II) ion and one fully deprotonated Isa-az-tmpz^{2-} ligand, as well as a strongly disordered DMF molecule which was removed with the SQUEEZE function in PLATON [24,25]. Each Zn(II) ion had a square-pyramidal coordination with Zn-O bond lengths between 2.024(2) and 2.046(2) Å in equatorial positions and a similarly long Zn-N bond of 2.039(2) Å in axial position. Two of these Zn(II) ions form a paddlewheel cluster connected through four isophthalate and two pyrazole units of six different linker molecules to a 3D network (Figure 2a). The isophthalate and pyrazole-ring plane are tilted by about 20° with respect to each other.

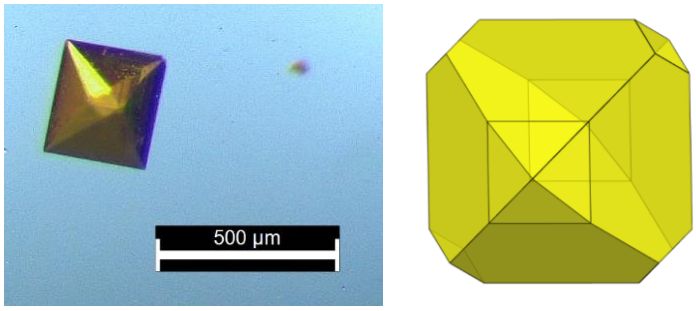

(**a**) (**b**)

Figure 1. (**a**) Crystal morphology of [Zn(isa-az-tmpz)]·~1–1.5 DMF and (**b**) the predicted crystal habit of a truncated octahedron with two square pyramids on top of two opposite trunks from the Bravais, Friedel, Donnay and Harker (BFDH) algorithm embedded in MERCURY [23].

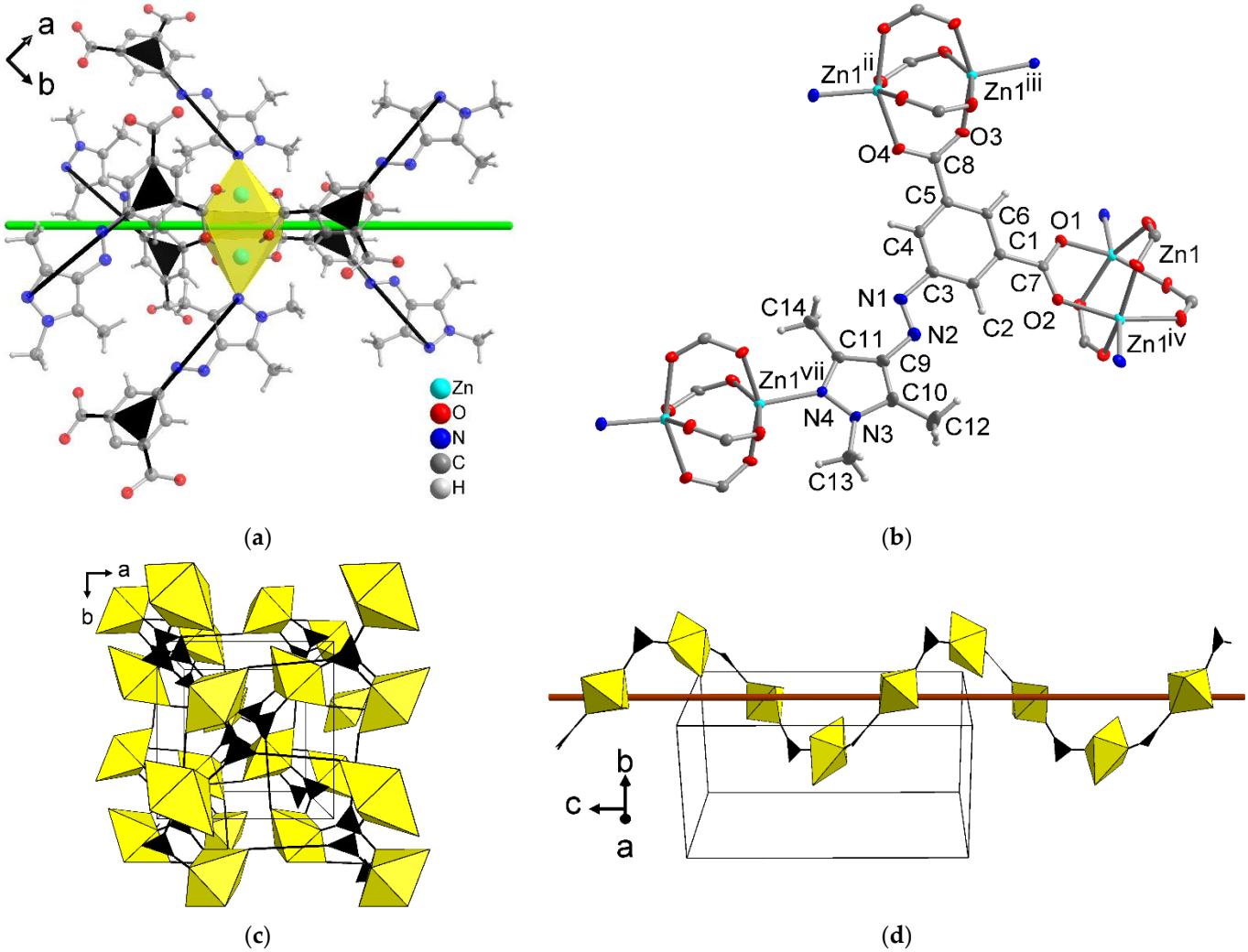

(**a**) (**b**)

(**c**) (**d**)

Figure 2. (**a**) Extended asymmetric unit of [Zn(Isa-az-tmpz)]·~1–1.5 DMF (50% thermal ellipsoids, H atoms with arbitrary radii). Symmetry transformations: (ii) −y + 3/2, x + 1/2, z − 1/4; (iii) x + 1/2, −y + 3/2, −z + 5/4; (iv) y, x, −z + 1; (vii) y − 1/2, −x + 1/2, z + 1/4. (**b**) Position of the Zn_2 paddlewheel cluster around the C2-axis (green). The paddlewheel unit was drawn as a yellow 6-c node and the Isa-az-tmpz^{2-} ligand is depicted as a black 3-c node. (**c**) 3D-network structure and (**d**) the 4_3-helix in [Zn(Isa-az-tmpz)] in nodal presentation.

Paddlewheel clusters are commonly found in Zn-MOFs, with Zn-HKUST-1 and SDU-1 being two examples [26,27]. These paddlewheel clusters can exhibit symmetries up to D_{4h} depending on the symmetries of the ligand and the molecules or ligands in axial positions. Due to the low symmetry of Isa-az-tmpz^{2-}, the clusters in the network [Zn(Isa-az-tmpz)] have a reduced C_2 symmetry without an inversion center or mirror faces (Figure 2b).

Each paddlewheel cluster was connected to six ligand molecules (Figure 2b), which in turn were linked to two further paddlewheel clusters to form a 3D-network (Figure 2c). This 3D-network can be separated into 2D-chains, consisting of the paddlewheel units interconnected through the isophthalate functionality of the ligand. As a result, these form a left-handed 4_3 or a right-handed 4_1 helix along the crystallographic 4_3 or 4_1 axis, respectively, which was colinear with the c-axis (Figure 2d).

The compound crystallizes in the chiral, enantiomorphic tetragonal space groups $P4_32_12$ or $P4_12_12$ as a conglomerate of crystals, with varying degrees of enantiomeric excess. The four investigated crystals (Table 1) were refined as inversion twins with ratios of about 7:3 and 6:4 or 4:6 and 2:8 of both enantiomorphic forms [28,29]. Thus, the individual investigated crystals were not enantiopure (homochiral) but only of enantiomeric excess. The formation of fourfold helices in isophthalate-MOFs was also seen in [Al(OH)(isophthalate)] (CAU-10-H, including benzene-functionalized derivatives) [30–32].

Table 1. Crystal data and structure refinement details of [Zn(Isa-az-tmpz)]·~1–1.5 DMF.

	Crystal 1a	**Crystal 1b**	**Crystal 2a**	**Crystal 2b**
CCDC no.	2192050	2192051	2192052	2192053
Device	Bruker Apex	Rigaku Synergy	Bruker Apex	Rigaku Synergy
Radiation	Mo Kα	Cu Kα	Mo Kα	Cu Kα
Wavelength (Å)	0.71073	1.54184	0.71073	1.54184
Chemical formula	$C_{14}H_{12}N_4O_4Zn$	$C_{14}H_{12}N_4O_4Zn$	$C_{14}H_{12}N_4O_4Zn$	$C_{14}H_{12}N_4O_4Zn$
M_r (g mol^{-1})	365.65	365.65	365.65	365.65
Crystal system, space group	Tetragonal, $P4_32_12$	Tetragonal, $P4_32_12$	Tetragonal, $P4_12_12$	Tetragonal, $P4_12_12$
Temperature (K)	100	100	140	100
a = b (Å)	12.8882 (9)	12.89036 (2)	12.9058 (6)	12.89103 (4)
c (Å)	25.421 (2)	25.44987 (7)	25.5686 (18)	25.47177 (13)
V (Å^3)	4222.6 (7)	4228.79 (2)	4258.7 (5)	4232.86 (3)
Z	8	8	8	8
μ (mm^{-1})	1.18	1.79	1.17	1.79
d_{calc} (g cm^{-3})	1.150	1.149	1.141	1.148
F (000)	1488	1488	1488	1488
Crystal size (mm)	0.27 × 0.25 × 0.22	0.49 × 0.43 × 0.34	0.02 × 0.02 × 0.02	0.35 × 0.29 × 0.18
Exp. abs. correct. (min/max)	0.8683/1.0000	0.95677/0.95677	0.8874/1.0000	0.97219/0.97219
meas., indep., obs. reflect.	17351, 4337, 4014	256848, 3776, 3774	54539, 4362, 4094	39328, 3781, 3730
parameters, restraints	212, 0	212, 0	212, 0	212, 0
R_{int}	0.030	0.050	0.055	0.037
$(\sin\theta/\lambda)_{max}$ (Å^{-1})	0.604	0.597	0.626	0.597
R, wR(F^2)	0.0215, 0.0516	0.0185, 0.0526	0.0252, 0.0586	0.0208, 0.0592
S [$F^2 > 2\sigma$ (F^2)] [a]	1.051	1.098	1.063	1.056
R, wR(F^2)	0.0244, 0.0524	0.0185, 0.0526	0.0283, 0.0598	0.0211, 0.0595
S [all data] [a]	1.051	1.098	1.063	1.056
$\Delta\rho$max., $\Delta\rho$min. (e Å^{-3}) [b]	0.24, -0.17	0.17; -0.24	0.69; -0.29	0.19; -0.29
Flack parameter [c]	0.298(11)	0.43 (2)	0.443 (13)	0.20 (3)
Squeeze solvent access. vol. (Å^3) [d]	1686	1744	1699	1756
Squeeze void count electrons [d]	438	496	478	480
approx. no. DMF molec. per formula unit [e]	1.4	1.5	1.5	1.5

[a] $R_1 = [\Sigma(|F_o| - |F_c|)/\Sigma|F_o|]$; $wR_2 = [\Sigma[w(F_o^2 - F_c^2)^2]/\Sigma[w(F_o^2)^2]]^{1/2}$. Goodness-of-fit $S = [\Sigma[w(F_o^2 - F_c^2)^2]/(n-p)]^{1/2}$. [b] Largest difference peak and hole. [c] Flack parameter [33–36]. [d] Per unit cell. [e] 40 electrons in a DMF molecule. Void count electrons/40/8(Z) = number of DMF per asymmetric unit (here equal formula unit). The squeezed DMF content was not included in d_{calc} and F(000).

A packing analysis of the network [Zn(Isa-az-tmpz)] shows the absence of π-π and C-H···π interactions within the structure [37]. The steric constraints of the three methyl groups on the pyrazolyl ring prevent such π-π interactions between the aromatic rings of the ligand. The network [Zn(Isa-az-tmpz)] follows the basic principles of the 'ligand–to–axial pillaring' strategy of the SBL approach consisting of a paddlewheel cluster, which can be described as an octahedral 6-c node and a T-shaped ligand, which works as a trigonal 3-c node. Deviating from the SBL approach, the topological analysis of the structure with the program ToposPro [38,39] and the Topcryst database [40,41] yielded the rare chiral **3,6T22**-topology as the underlying net, instead of the expected **rtl**-topology (Figure 3).

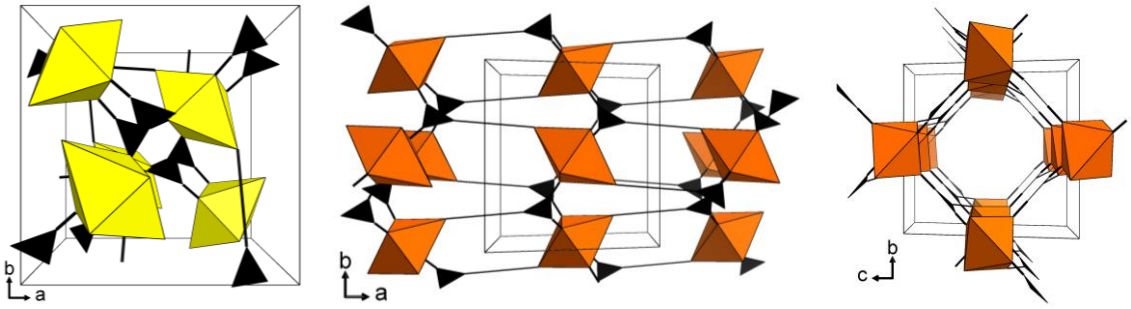

(**a**) (**b**)

Figure 3. (**a**) 3-c and 6-c connectivity of the ligand and the paddlewheel unit in the unit cell of **3,6T22**-[Zn(Isa-az-tmpz)]·~1–1.5 DMF presented in this work compared to (**b**) the literature reported structure of **rtl**-[Zn(HIsa-az-dmpz)] in two viewing directions. The structure for **rtl**-[Zn(HIsa-az-dmpz)] was re-drawn from the cif file with CSD-number 1908794 deposited in the CCDC [13].

To date, the **3,6T22**-topology has been reported in multiple G⊂Cd(L)$_2$ (G = guest molecule; L = 4-amino-3,5-bis(4-pyridyl-3-phenyl)-1,2,4-triazole) host@guest complexes, reported by Liu et al. [42,43]. More recently, the **3,6T22**-topology has been observed in the Cd- and Fe-based MOFs [(Me$_2$NH$_2$)Cd$_3$(OH)(H$_2$O)$_3$(Tatab)$_2$] (Tatab = 4,4′,4″-s-triazin-1,3,5-triyltri-p-amino-benzoate) and [Fe$_2$M(Bptc)] (M = Fe, Co, Ni, Zn; Bptc = biphenyl-3,4′,5-tricarboxylate), synthesized by Liu et al. [44] and Wang et al. [45], respectively. The other **3,6T22** MOFs all had a 3c-linker node connected to an octahedrally distorted 6c-metal (SBU) node. In G⊂Cd(L)$_2$ the SBU distortion originates from four pyridyl and two triazole donors around the six-coordinated Cd atom (see Supplementary Materials Figure S13a). In [(Me$_2$NH$_2$)Cd$_3$(OH) (H$_2$O)$_3$(Tatab)$_2$] and [Fe$_2$M(Bptc)] the trinuclear {M$_3$(μ$_3$-O)(H$_2$O)$_3$(O$_2$C-)$_6$} SBU was a trigonal prism, which also represents a distortion from an octahedron (Figure S13b,c). In [Zn(Isa-az-tmpz)]·~1–1.5 DMF the dinuclear paddlewheel SBU gave rise to a tetragonally distorted, elongated octahedron (Figure S13d). In G⊂Cd(L)$_2$, [Fe$_2$M(Bptc)] and [Zn(Isa-az-tmpz)] the 3c-linker node also was asymmetric, as it had short and long bonds to the SBU (Figure S13a,c,d). Only the Tatab^{3-} linker was trigonal symmetric (Figure S13b). The Bptc^{3-} linker was also a T-shaped linker like Isa-az-tmpz^{2-}, albeit with a tricarboxylate donor set. To the best of our knowledge, this was the first work that shows that this topology can be achieved using a T-shaped bifunctional pyrazole–dicarboxylate ligand following the 'ligand-to-axial pillaring' approach.

The solvent-depleted 3D network [Zn(Isa-az-tmpz)] has potential porosity from the identical perpendicular corrugated channel systems along the a- and b-axes with trigonal cross-selections of about 6 × 4 Å, which could only accommodate a sphere of about 3 Å diameter (considering the van der Waals surface) (Figure 4). A solvent accessible volume (SAV) of 1661 Å^3 or 39 vol% out of the unit cell volume of 4223 Å^3 was calculated with PLATON [24] for the solvent-depleted structure. The SAV of 1661 Å^3 calculates into a specific pore volume of 0.34 cm^3 g^{-1} according to (SAV × N$_A$)/(Z × M$_{asym\ unit}$); (N$_A$ = Avogadro's constant: 6.022·10^{23} mol^{-1}, Z = number of asymmetric formula units, M$_{asym\ unit}$ = molecular weight of asymmetric formula unit in g mol^{-1}; see Table S1).

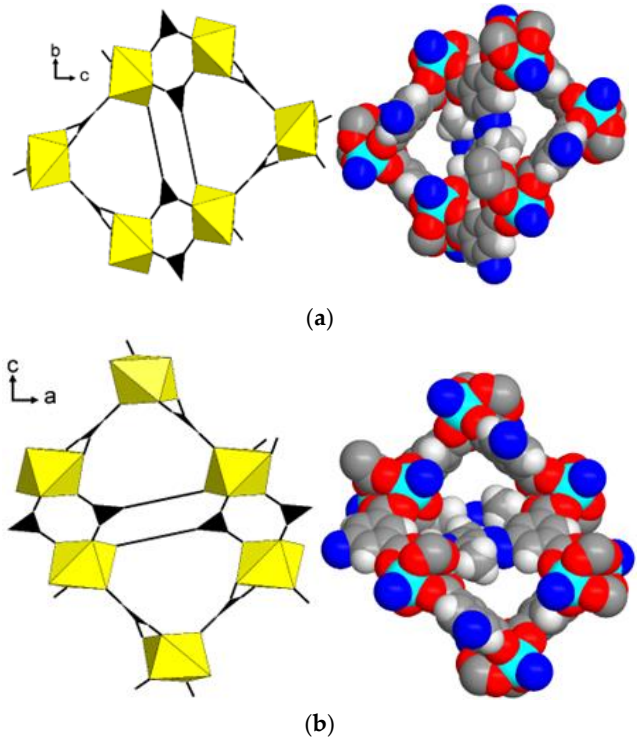

Figure 4. Channels in solvent-depleted [Zn(Isa-az-tpmz)] along the (**a**) a- and (**b**) b-axis in schematic and space-filling representation showing the corrugated trigonal channels.

The representative nature of the selected crystal from [Zn(Isa-az-tmpz)]·~1–1.5 DMF and the phase-purity of the bulk material was confirmed by a positive match between the simulated powder X-ray diffraction (PXRD) pattern and experimental pattern of the as-synthesized material (Figure 5a,b). For the prospective gas sorption studies, DMF was exchanged with acetone, and afterwards the material has been dried with supercritical CO_2. At this stage, no phase change or loss of crystallinity in the bulk material could be observed with PXRD (Figure 5c,d). The solvent exchange does not influence the general structure of the MOF, as the peak positions remained unchanged. However, the difference in electron density in the pores from the solvent exchange can affect the peak intensities [46].

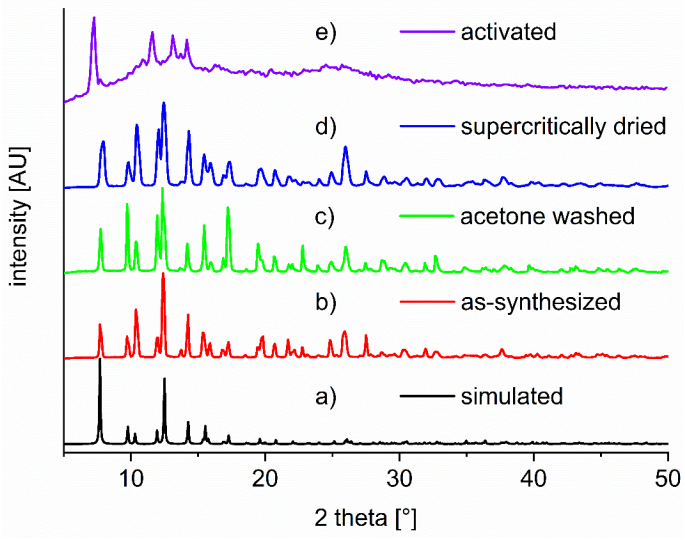

Figure 5. Comparison of the simulated (**a**) and experimental PXRDs of [Zn(Isa-az-tmpz)] after sequential activation steps (**b**–**e**). The "activated" material (**e**) was derived from the supercritically dried sample (**d**) through additional heating of the material for 3 h at 120 °C under high vacuum.

Thermal analysis of the supercritically dried (sc-dried) sample with TGA showed only a slightly decreased mass loss compared to the acetone-washed sample. While in one sample, the solvent could nearly be completely removed according to TGA (Figure S8), in another sample about 15 mass% of DMF up to 250 °C remained in both the acetone-washed and the subsequently sc-dried sample (Figure S9). Hence, the sc-dried material was additionally heated for 3 h at 120 °C under high vacuum to further activate the sample before measurement, which yielded a material with low crystallinity (Figure 5e). This indicates a partial collapse of the 3D network structure during solvent removal under too harsh conditions. Following a volumetric nitrogen sorption experiment at 77 K, no gas uptake could be seen. A sorption measurement with the sc-dried sample, activated under high vacuum at room temperature, had a similarly low N_2 uptake (Figure S10).

Due to the low nitrogen uptake and small channel size of solvent-depleted [Zn(Isaaz-tmpz)], sorption experiments at 87 K for argon (Ar) and hydrogen (H_2) and at 195 K for carbon dioxide were collected for the sc-dried and additionally heated material (3 h, 120 °C). While the Ar sorption measurement showed low gas uptake (Figure S11), the H_2 sorption yielded an isotherm similar to type I(b) isotherms for microporous materials, with a total uptake of 2 mmol·g^{-1} (Figure 6) [47]. The CO_2 sorption experiment showed the microporous nature of the material by also providing a type I(b) isotherm and a significant CO_2 uptake, from which a Langmuir surface area of 588 m^2·g^{-1} and a BET surface area of 496 m^2·g^{-1} was calculated. Assuming the validity of the Gurvich rule, the division of (specific CO_2 amount adsorbed in g g^{-1} with the CO_2 saturation pressure at 195 K of 1.00 bar)/(density of liquid CO_2 adsorbate with ρ_{CO2}(195 K) = 1.08 g cm^{-3}) gave a pore volume of 0.22 cm^3 g^{-1} (the uptake of 120 cm^3 g^{-1} at STP at 1 bar is 5.4 mmol g^{-1} or 2.4 g g^{-1}) [48]. The difference in gas uptake between N_2, Ar, H_2 and CO_2 correlates with the kinetic diameters (3.64, 3.40, 2.89 and 3.30 Å, respectively), with the cryogenic temperatures for N_2 (77 K) and Ar (87 K) and the ultramicroporous (<7 Å pore size) nature of the framework. The diffusion of N_2 molecules and Ar atoms into small pores was then very slow, while kinetic inhibition was less severe for smaller H_2 molecules and for CO_2 at 195 K.

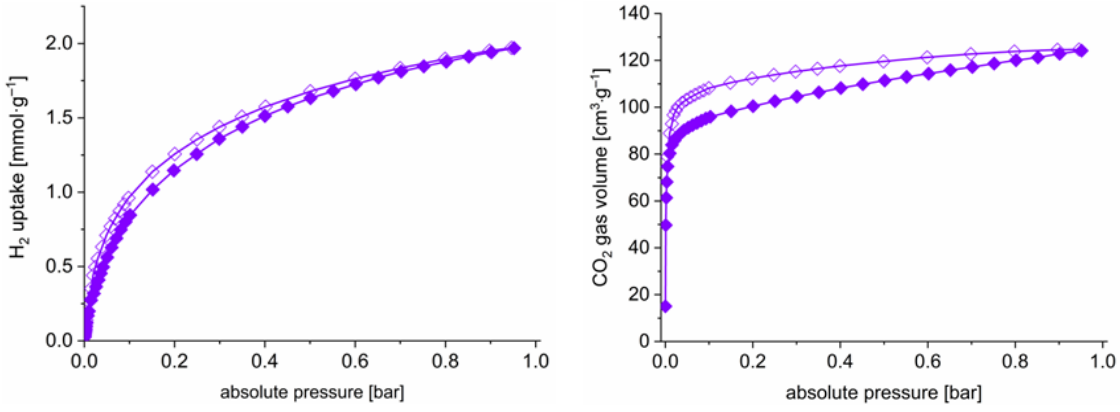

Figure 6. (**a**) Volumetric H_2 (at 87 K,) and (**b**) CO_2 (at 195 K) sorption isotherms of activated [Zn(Isaaz-tmpz)] (sc-dried and additionally heated for 3 h at 120 °C) (filled symbols for adsorption, empty symbols for desorption).

3. Materials and Methods

3.1. Materials and Characterization

All reagents were obtained from commercial sources and used without further purification. C, H, N analyses were executed on a vario MICRO cube from Elementar Analysentechnik. ^{1}H-NMR and ^{13}C-NMR spectra were measured on a Bruker Avance III-300. IR-spectra were recorded on a Bruker Tensor 37 IR spectrometer equipped with an attenuated total reflection (ATR) unit (Platinum ATR-QL, Diamond). Electrospray ionization-mass

spectra (ESI-MS) were measured on a Finnigan LCQ Deca Thermoquest in acetone, electron ionization-mass spectra (EI-MS) on a TSQ 7000 Finnigan MAT. Thermogravimetric analysis was executed on a Netzsch TG 209 F3 Tarsus in the range from 30 °C to 600 °C with a heating rate of 5 K min^{-1} under a nitrogen atmosphere. Powder X-ray diffraction (PXRD) patterns were measured on a Bruker D2 Phaser powder diffractometer with a flat silicon, low background sample holder, at 30 kV, 10 mA with Cu-Kα radiation (λ = 1.5418 Å). The most intense reflection in each diffractogram was normalized to 1. The simulated PXRD pattern has been calculated with MERCURY software [23]. Supercritical drying was carried out on a Leica EMPCD 300 over 99 exchange cycles with CO_2. Adsorption data for N_2 at 77 K (liquid nitrogen bath) was collected on a Quantachrome NOVA 4000 gas adsorption analyzer. Additional sorption experiments for Ar and H_2 at 87 K (Quantachrome CRYOCOOLER) and CO_2 at 195 K (Quantachrome CRYOCOOLER), respectively, were conducted on a Quantachrome Autosorb iQ MP. The supercritically dried sample was used and outgassed before the gas sorption measurements were taken, either at room temperature or at 120 °C for a minimum of 3 h.

3.2. Single Crystal X-ray Diffraction

Suitable crystals were carefully selected under a polarized-light microscope, covered in protective oil and mounted on a cryo-loop.

For crystals 1a and 2a, the data were collected on a Bruker Kappa APEX 2 CCD X-ray diffractometer with a microfocus sealed tube, Mo-Kα radiation (λ = 0.71073 Å), and a multi-layer mirror monochromator; data collection took place at 100 ± 2 K (crystal 1a) or 140 ± 2 (crystal 2a) using ω-scans, cell refinement with APEX2 [49], data reduction with SAINT [50] and experimental adsorption correction with SADABS [51].

For crystals 1b and 2b, the single crystal diffraction data were collected using a Rigaku XtaLAB Synergy S four circle diffractometer with a Hybrid Pixel Array Detector and a PhotonJet X-ray source for Cu-Kα radiation (λ = 1.54184 Å), with a multilayer mirror monochromator. Data collection took place at 100.0 ± 0.1 K using ω-scans. Data reduction and absorption correction were performed with CrysAlisPro 1.171.41.105a [52].

Structure analysis and refinement: The structures were solved by direct methods (SHELXT-2015), full-matrix least-squares refinements on F^2 were executed using the SHELXL-2017/1 program package [53,54]. All hydrogen atoms were positioned geometrically (with C–H = 0.95 Å for aromatic CH and C–H = 0.98 Å for CH_3) and refined using riding models (AFIX 43 and 137 with $U_{iso(H)}$ = 1.2 U_{eq} (CH) and 1.5 U_{eq} (CH_3)).

Highly disordered solvent molecules were either masked with the SQUEEZE option in PLATON [24,25] (crystals 1a and 2a) or by using the solvent mask feature as implemented in OLEX 2.1.3 [55] (crystals 1b and 2b). Crystal data and details on the structure refinement are provided in Table 1. Details about selected bond distances and angles are provided in Table S2 in the supporting information. Graphics were drawn with the program DIAMOND [56].

The crystallographic data (excluding structure factors) for the structures were deposited with the Cambridge Crystallographic Data Centre (CCDC-numbers 2192050-2192053) and can be obtained free of charge via www.ccdc.cam.ac.uk/data_request/cif.

3.3. Synthesis of H_2Isa-az-tmpz

The ligand was synthesized following a modified previously reported procedure [13]. Dimethyl 5-(2-(2,4-dioxopentan-3-ylidene)hydrazineyl)isophthalate (2) was obtained via a Japp-Klingemann reaction of dimethyl 5-aminoisophthalate (1) with acetylacetone. Compound 2 was converted with methyl hydrazine into dimethyl 5-(2-(1,3,5-trimethyl-1H-pyrazol-4-yl)azo)isophthalate (3), which was later deprotected under basic conditions to obtain 5-(2-(1,3,5-trimethyl-1H-pyrazol-4-yl)azo)isophthalic acid (H_2Isa-az-tmpz) (4) as a new ligand in 76% yield over three steps (Scheme 2). The detailed synthetic procedure and analysis can be found in the SI.

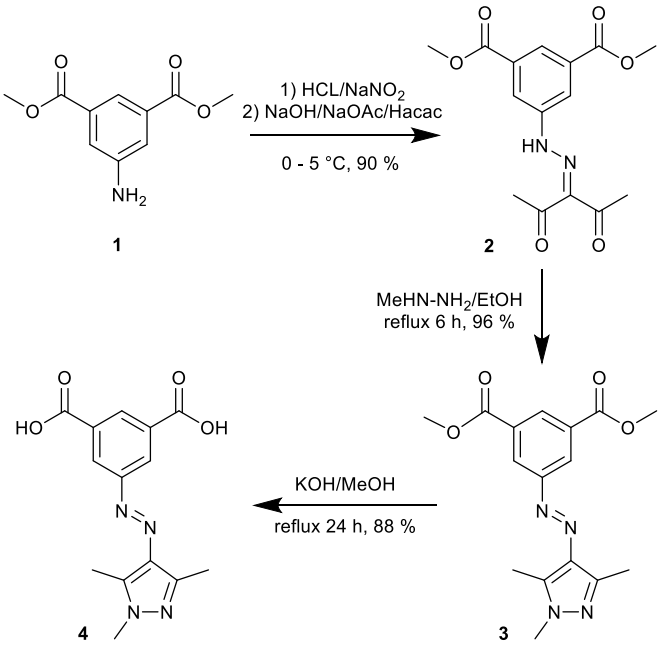

Scheme 2. Reaction scheme for the synthesis of H_2Isa-az-tmpz.

3.4. Synthesis of [Zn(Isa-az-tmpz)]·~1–1.5 DMF

In a Pyrex tube, 9.7 mg (0.032 mmol) of H_2Isa-az-tmpz and 16.8 mg (0.064 mmol) of $Zn(NO_3)_2{\cdot}4\ H_2O$ were dissolved in 2 mL of DMF. The tube with the yellow solution was placed into a preheated oven at 80 °C for 72 h to obtain yellow block-shaped crystals. The mother liquor was then exchanged against fresh DMF (2 mL) to prevent further growth and stored at RT until single crystal analysis.

On a larger scale, 100 mg (0.33 mmol) of H_2Isa-az-tmpz dissolved in 10 mL of DMF was added to a solution of 170 mg (0.65 mmol) $Zn(NO_3)_2{\cdot}4\ H_2O$ in 10 mL of DMF. The same temperature program used for the single crystal synthesis was applied. The obtained as-synthesized polycrystalline yellow material was washed with DMF (10 mL). The solvent was replaced once a day for three days followed by acetone (10 mL), which also had the solvent replaced once a day for three days. Subsequently, the sample was activated via supercritical drying with CO_2 yielding 81.4 mg (67 %) of a yellow precipitate as the activated material.

Calculated for as-synthesized [Zn(Isa-az-tmpz)]·1 DMF ($ZnC_{17}H_{19}N_5O_5$), C 46.54%, H 4.37%, N 15.96%; found C 46.36%, H 4.37%, N 15.66%;

Calculated for activated [Zn(Isa-az-tmpz)] (no DMF) ($ZnC_{14}H_{14}N_4O_4$), C 45.99%, H 3.31%, N 15.32%; found for sample 1: C 45.95%, H 4.37%, N 14.97%; sample 2: C 46.60%, H 3.72%, N 14.56%.

IR for activated [Zn(Isa-az-tmpz)] [cm^{-1}]: 1677 (w), 1648 (s, COO^-), 1560 (w), 1521 (w), 1438 (m, CH_3), 1372 (s, C-N), 1254 (w), 1233 (w), 1091 (w), 1061 (w), 1040 (w), 1008 (w), 974 (w), 921 (w), 865 (w), 805 (w), 778 (m, Ar-H), 717 (m, Ar-H), 682 (m, Ar-H), 635 (w), 606 (w), 588 (w).

4. Conclusions

We presented the synthesis of the MOF [Zn(Isa-az-tmpz)]·~1–1.5 DMF with the rare chiral **3,6T22**-topology through the reaction of zinc nitrate with the newly synthesized T-shaped linker 5-(2-(1,3,5-trimethyl-1H-pyrazol-4-yl)azo)isophthalic acid (H_2Isa-az-tmpz) in DMF at elevated temperatures. Even though the deprotonated form Isa-az-tmpz^{2-} fulfills the general principles of the 'ligand-to-axial pillaring' strategy of the supramolecular building layer (SBL) approach, leading to a 3,6-c connected MOF, the resulting topology does not follow the SBL approach and cannot be described through this. Contrary to the related coordination polymer **rtl**-[Zn(HIsa-az-dmpz)], which could not be activated to its

porous material, the porosity for the ultramicroporous MOF (pore diameters less than 7 Å) **3,6T22**-[Zn(Isa-az-tmpz)]·~1–1.5 DMF could be assessed with H_2 at 87 K and with CO_2 at 195 K but not with N_2 and Ar under the cryogenic conditions of 77 and 87 K, respectively. Overall, this work can be considered a starting point to obtain chiral and potentially porous MOFs using bifunctional and T-shaped pyrazole-carboxylate ligands. Chiral MOFs are promising materials for enantioselective adsorption, separation and catalysis [20–22].

Supplementary Materials: The following supporting information can be downloaded at: https://www.mdpi.com/article/10.3390/molecules27175374/s1. Synthesis of H_2Isa-az-tmpz, results of ^{1}H-NMR, ^{13}C-NMR, EA and EI/ESI-MS. Figure S1. ^{1}H-NMR spectrum of dimethyl 5-(2-(2,4-dioxopentan-3-ylidene)hydrazineyl)-isophthalate in $CDCl_3$. Figure S2. ^{13}C-NMR spectrum of dimethyl 5-(2-(2,4-dioxopentan-3-ylidene)hydrazineyl)-isophthalate in $CDCl_3$. Figure S3. ^{1}H-NMR spectrum of dimethyl 5-(2-(1,3,5 trimethyl-1H-pyrazol-4 yl)azo)-isophthalate in $CDCl_3$. Figure S4. ^{13}C-NMR spectrum of dimethyl 5-(2-(1,3,5 trimethyl-1H-pyrazol-4 yl)azo)-isophthalate in $CDCl_3$. Figure S5. ^{1}H-NMR spectrum of H_2Isa-az-tmpz in DMSO-d6. Figure S6. ^{13}C-NMR spectrum of H_2Isa-az-tmpz in DMSO-d6. Figure S7. Complete IR-spectra (left) of [Zn(Isa-az-tmpz)]·~1–1.5 DMF and H_2Isa-az-tmpz and a cutout (right) focusing on the range from 1800 to 500 cm^{-1}. Figure S8. Crystals of [Zn(Isa-az-tmpz)]·~1–1.5 DMF obtained from a single crystal synthesis. Figure S9. TGA of [Zn(isa-az-tmpz)] after sequential activation steps. The "activated" material was derived from the supercritically dried sample through additional heating for 3 h at 120 °C under high vacuum. Figure S10. Volumetric nitrogen sorption measurements of [Zn(isa-az-tmpz)] activated at room temperature (RT) and 120 °C. Figure S11. Volumetric argon sorption measurement of [Zn(isa-az-tmpz)] activated at 120 °C. Table S1. Theoretical surface area and pore volume of [Zn(isa-az-tmpz)] [Mercury 'void' calculation [23], Platon 'Calc Void' [24,25], CrystalExplorer 'Crystal voids' calculation [57,58]]. Topology analysis for [Zn(isa-az-tmpz)] with ToposPro [38–41]. Figure S12. Hydrogen bonds in [Zn(Isa-az-tmpz)]. Symmetry transformations: (vii) y-1/2, -x + 1/2, z + 1/4; (viii) x, y-1, z; (ix) -y + 1, -x, -z + 3/2; (x) x-1/2, -y + 1/2, -z + 5/4. Figure S13. Representations of the metal-linker connectivities in the **3,6T22** MOFs (a) G⊂$Cd(L)_2$ [42,43], (b) [$(Me_2NH_2)Cd_3(OH)$ $(H_2O)_3(Tatab)_2$] [44], (c) [$Fe_2M(Bptc)$] [45] and (d) [Zn(Isa-az-tmpz)] (this work) The metal SBUs are drawn as yellow 6-c nodes and the linkers are depicted as black 3-c nodes. (L = 4-amino-3,5-bis(4-pyridyl-3-phenyl)-1,2,4-triazole, Tatab = 4,4′,4″-s-triazin-1,3,5-triyltri-p-amino-benzoate, Bptc = biphenyl-3,4′,5-tricarboxylate). Table S2. Selected bond lengths [Å] and angles [°] for [Zn(isa-az-tmpz)] in Crystal 1a. Table S3. Hydrogen bond lengths [Å] and angles [°] for [Zn(isa-az-tmpz)] in Crystal 1a.

Author Contributions: Conceptualization, C.J., D.W and S.M.; methodology, D.W.; validation, D.W.; formal analysis, D.W.; investigation, D.W., S.M., M.-A.C., R.O.; resources, C.J.; Data Curation, D.W.; writing—original draft, D.W.; writing—review and editing, C.J.; visualization, D.W. and C.J.; supervision, C.J.; project administration, C.J.; funding acquisition, C.J. All authors have read and agreed to the published version of the manuscript.

Funding: This research received no external funding.

Institutional Review Board Statement: Not applicable.

Informed Consent Statement: Not applicable.

Data Availability Statement: The data presented in this study are available on request from the corresponding author.

Conflicts of Interest: The authors declare that they have no known competing financial interests or personal relationships that could have appeared to influence the work reported in this paper.

References

1. Safaei, M.; Foroughi, M.M.; Ebrahimpoor, N.; Jahani, S.; Omidi, A.; Khatami, M. A review on metal-organic frameworks: Synthesis and applications. *TrAC Trends Anal. Chem.* **2019**, *118*, 401–425. [CrossRef]
2. Jiao, L.; Seow, J.Y.R.; Skinner, W.S.; Wang, Z.U.; Jiang, H.-L. Metal–organic frameworks: Structures and functional applications. *Mater. Today* **2019**, *27*, 43–68. [CrossRef]
3. Kirchon, A.; Feng, L.; Drake, H.F.; Joseph, E.A.; Zhou, H.-C. From fundamentals to applications: A toolbox for robust and multifunctional MOF materials. *Chem. Soc. Rev.* **2018**, *47*, 8611–8638. [CrossRef]

4. Guillerm, V.; Kim, D.; Eubank, J.F.; Luebke, R.; Liu, X.; Adil, K.; Lah, M.S.; Eddaoudi, M. A supermolecular building approach for the design and construction of metal-organic frameworks. *Chem. Soc. Rev.* **2014**, *43*, 6141–6172. [CrossRef] [PubMed]
5. Dybtsev, D.N.; Chun, H.; Kim, K. Rigid and flexible: A highly porous metal-organic framework with unusual guest-dependent dynamic behavior. *Angew. Chem. Int. Ed.* **2004**, *43*, 5033–5036. [CrossRef]
6. He, H.; Dou, J.; Li, D.; Ma, H.; Sun, D. Synthesis, crystal structures and properties of four topological structures based on 2,3,5,6-tetramethyl-1,4-benzenedicarboxylate acid and bipyridine ligands. *CrystEngComm* **2011**, *13*, 1509–1517. [CrossRef]
7. Zhang, L.-P.; Ma, J.-F.; Yang, J.; Pang, Y.-Y.; Ma, J.-C. Series of 2D and 3D coordination polymers based on 1,2,3,4-benzenetetracarboxylate and N-donor ligands: Synthesis, topological structures, and photoluminescent properties. *Inorg. Chem.* **2010**, *49*, 1535–1550. [CrossRef] [PubMed]
8. Ma, B.-Q.; Mulfort, K.L.; Hupp, J.T. Microporous pillared paddle-wheel frameworks based on mixed-ligand coordination of zinc ions. *Inorg. Chem.* **2005**, *44*, 4912–4914. [CrossRef]
9. Seki, K.; Takamizawa, S.; Mori, W. Design and Gas Adsorption Property of a Three-Dimensional Coordination Polymer with a Stable and Highly Porous Framwork. *Chem. Lett.* **2001**, *30*, 332–333. [CrossRef]
10. Eubank, J.F.; Wojtas, L.; Hight, M.R.; Bousquet, T.; Kravtsov, V.C.; Eddaoudi, M. The next chapter in MOF pillaring strategies: Trigonal heterofunctional ligands to access targeted high-connected three dimensional nets, isoreticular platforms. *J. Am. Chem. Soc.* **2011**, *133*, 17532–17535. [CrossRef]
11. Liu, X.; Oh, M.; Lah, M.S. Size- and shape-selective isostructural microporous metal-organic frameworks with different effec-tive aperture sizes. *Inorg. Chem.* **2011**, *50*, 5044–5053. [CrossRef] [PubMed]
12. Wei, Y.-S.; Lin, R.-B.; Wang, P.; Liao, P.-Q.; He, C.-T.; Xue, W.; Hou, L.; Zhang, W.-X.; Zhang, J.-P.; Chen, X.-M. New porous coordination polymers based on expanded pyridyl-dicarboxylate ligands and a paddle-wheel cluster. *CrystEngComm* **2014**, *16*, 6325–6330. [CrossRef]
13. Millan, S.; Gil-Hernández, B.; Milles, E.; Gökpinar, S.; Makhloufi, G.; Schmitz, A.; Schlüsener, C.; Janiak, C. rtl-M-MOFs (M = Cu, Zn) with a T-shaped bifunctional pyrazole-isophthalate ligand showing flexibility and S-shaped Type F-IV sorption iso-therms with high saturation uptakes for M = Cu. *Dalton Trans.* **2019**, *48*, 8057–8067. [CrossRef]
14. Wang, S.; Wei, Z.-W.; Zhang, J.; Jiang, L.; Liu, D.; Jiang, J.-J.; Si, R.; Su, C.-Y. Framework disorder and its effect on selective hysteretic sorption of a T-shaped azole-based metal-organic framework. *IUCrJ* **2019**, *6*, 85–95. [CrossRef] [PubMed]
15. Bryant, M.R.; Burrows, A.D.; Fitchett, C.M.; Hawes, C.S.; Hunter, S.O.; Keenan, L.L.; Kelly, D.J.; Kruger, P.E.; Mahon, M.F.; Richardson, C. The synthesis and characterisation of coordination and hydrogen-bonded networks based on 4-(3,5-dimethyl-1H-pyrazol-4-yl)benzoic acid. *Dalton Trans.* **2015**, *44*, 9269–9280. [CrossRef] [PubMed]
16. Gao, W.-Y.; Cai, R.; Pham, T.; Forrest, K.A.; Hogan, A.; Nugent, P.; Williams, K.; Wojtas, L.; Luebke, R.; Weseliński, Ł.J.; et al. Remote Stabilization of Copper Paddlewheel Based Molec-ular Building Blocks in Metal–Organic Frameworks. *Chem. Mater.* **2015**, *27*, 2144–2151. [CrossRef]
17. Sussardi, A.; Marshall, R.J.; Moggach, S.A.; Jones, A.C.; Forgan, R.S. Photophysics of Azobenzene Constrained in a UiO Met-al-Organic Framework: Effects of Pressure, Solvation and Dynamic Disorder. *Chem. Eur. J.* **2021**, *27*, 14871–14875. [CrossRef]
18. Geng, J.; Liu, K.; Liang, Y.-Y.; Yu, J.; Hu, K.-Q.; Yuan, L.-H.; Feng, W.; Chai, Z.-F.; Mei, L.; Shi, W.-Q. An Azobenzene-Modified Photoresponsive Thorium-Organic Framework: Monitoring and Quantitative Analysis of Reversible trans-cis Photoisomeri-zation. *Inorg. Chem.* **2021**, *60*, 8519–8529. [CrossRef]
19. Khayyami, A.; Philip, A.; Multia, J.; Karppinen, M. Composition-tuned metal-organic thin-film structures based on pho-toswitchable azobenzene by ALD/MLD. *Dalton Trans.* **2020**, *49*, 11310–11316. [CrossRef]
20. Gong, W.; Chen, Z.; Dong, J.; Liu, Y.; Cui, Y. Chiral Metal-Organic Frameworks. *Chem. Rev.* **2022**, *122*, 9078–9144. [CrossRef]
21. Verma, G.; Mehta, R.; Kumar, S.; Ma, S. Metal-Organic Frameworks as a New Platform for Enantioselective Separations. *Isr. J. Chem.* **2021**, *61*, 708–726. [CrossRef]
22. Dhurjad, P.; Dharalam, C.S.; Ali, N.; Kumari, N.; Sonti, R. Metal-organic frameworks in chiral separation of pharmaceuticals. *Chirality* **2022**. [CrossRef] [PubMed]
23. Macrae, C.F.; Sovago, I.; Cottrell, S.J.; Galek, P.T.A.; McCabe, P.; Pidcock, E.; Platings, M.; Shields, G.P.; Stevens, J.S.; Towler, M.; et al. Mercury 4.0: From visualization to analysis, design and prediction. *J. Appl. Crystallogr.* **2020**, *53*, 226–235. [CrossRef] [PubMed]
24. Spek, A.L. *PLATON—A Multipurpose Crystallographic Tool*, Windows Implementation, Version 270519. Farrugia, L.J., Ed.; University of Glasgow, Scotland, UK. 2019.
25. Spek, A.L. Structure validation in chemical crystallography. *Acta Crystallogr. D Biol. Crystallogr.* **2009**, *65*, 148–155. [CrossRef]
26. Feldblyum, J.I.; Liu, M.; Gidley, D.W.; Matzger, A.J. Reconciling the discrepancies between crystallographic porosity and guest access as exemplified by Zn-HKUST-1. *J. Am. Chem. Soc.* **2011**, *133*, 18257–18263. [CrossRef]
27. Zhao, X.; Wang, X.; Wang, S.; Dou, J.; Cui, P.; Chen, Z.; Sun, D.; Wang, X.; Sun, D. Novel Metal–Organic Framework Based on Cubic and Trisoctahedral Supermolecular Building Blocks: Topological Analysis and Photoluminescent Property. *Cryst. Growth Des.* **2012**, *12*, 2736–2739. [CrossRef]
28. Flack, H.D. Chiral and Achiral Crystal Structures. *Helv. Chim. Acta* **2003**, *86*, 905–921. [CrossRef]
29. A chiral space group needs to have an element from one of the following four pairs of enantiomorphous screw rotations: {31, 32}, {41, 43}, {61, 65}, {62, 64}. Only 22 out of the 230 space groups are chiral. A crystal structure in P21 is chiral but the space group itself is achiral since it does not form one member of an enantiomorphous pair.

30. Reinsch, H.; van der Veen, M.A.; Gil, B.; Marszalek, B.; Verbiest, T.; de Vos, D.; Stock, N. Structures, Sorption Characteristics, and Nonlinear Optical Properties of a New Series of Highly Stable Aluminum MOFs. *Chem. Mater.* **2013**, *25*, 17–26. [CrossRef]
31. Reinsch, H.; Waitschat, S.; Stock, N. Mixed-linker MOFs with CAU-10 structure: Synthesis and gas sorption characteristics. *Dalton Trans.* **2013**, *42*, 4840–4847. [CrossRef]
32. Fröhlich, D.; Pantatosaki, E.; Kolokathis, P.D.; Markey, K.; Reinsch, H.; Baumgartner, M.; van der Veen, M.A.; de Vos, D.E.; Stock, N.; Papadopoulos, G.K.; et al. Water adsorption behaviour of CAU-10-H: A thorough investigation of its structure–property relationships. *J. Mater. Chem. A* **2016**, *4*, 11859–11869. [CrossRef]
33. Flack, H.D. On enantiomorph-polarity estimation. *Acta. Crystallogr. Sect. A Found. Crystallogr.* **1983**, *39*, 876–881. [CrossRef]
34. Flack, H.D.; Bernardinelli, G. Absolute structure and absolute configuration. *Acta. Crystallogr. Sect. A Found. Crystallogr.* **1999**, *A55*, 908–915. [CrossRef] [PubMed]
35. Flack, H.D.; Bernardinelli, G. The use of X-ray crystallography to determine absolute configuration. *Chirality* **2007**, *20*, 681–690. [CrossRef] [PubMed]
36. Flack, H.D.; Sadki, M.; Thompson, A.L.; Watkin, D.J. Practical applications of averages and differences of Friedel opposites. *Acta. Crystallogr. Sect. A Found. Crystallogr.* **2011**, *67*, 21–34. [CrossRef]
37. Janiak, C. A critical account on π–π stacking in metal complexes with aromatic nitrogen-containing ligands. *J. Chem. Soc. Dalton Trans.* **2000**, 3885–3896. [CrossRef]
38. Blatov, V.A.; Shevchenko, A.P.; Proserpio, D.M. Applied Topological Analysis of Crystal Structures with the Program Package ToposPro. *Cryst. Growth Des.* **2014**, *14*, 3576–3586. [CrossRef]
39. Alexandrov, E.V.; Blatov, V.A.; Kochetkov, A.V.; Proserpio, D.M. Underlying nets in three-periodic coordination polymers: Topology, taxonomy and prediction from a computer-aided analysis of the Cambridge Structural Database. *CrystEngComm* **2011**, *13*, 3947. [CrossRef]
40. Alexandrov, E.V.; Shevchenko, A.P.; Blatov, V.A. Topological Databases: Why Do We Need Them for Design of Coordination Polymers? *Cryst. Growth Des.* **2019**, *19*, 2604–2614. [CrossRef]
41. Blatov, V.A.; Proserpio, D.M. Topological relations between three-periodic nets. II. Binodal nets. *Acta. Crystallogr. A Found. Crystallogr.* **2009**, *65*, 202–212. [CrossRef]
42. Liu, Q.-K.; Ma, J.-P.; Dong, Y.-B. Reversible adsorption and complete separation of volatile chlorocarbons based on a Cd(II)-triazole MOF in a single-crystal-to-single-crystal fashion. *Chem. Commun.* **2011**, *47*, 12343–12345. [CrossRef]
43. Liu, Q.-K.; Ma, J.-P.; Dong, Y.-B. Adsorption and separation of reactive aromatic isomers and generation and stabilization of their radicals within cadmium(II)-triazole metal-organic confined space in a single-crystal-to-single-crystal fashion. *J. Am. Chem. Soc.* **2010**, *132*, 7005–7017. [CrossRef] [PubMed]
44. Liu, B.-H.; Liu, D.-X.; Yang, K.-Q.; Dong, S.-J.; Li, W.; Wang, Y.-J. A new cluster-based metal-organic framework with triazine backbones for selective luminescent detection of mercury(II) ion. *Inorg. Chem. Commun.* **2018**, *90*, 61–64. [CrossRef]
45. Wang, X.-L.; Dong, L.-Z.; Qiao, M.; Tang, Y.-J.; Liu, J.; Li, Y.; Li, S.-L.; Su, J.-X.; Lan, Y.-Q. Exploring the Performance Im-provement of the Oxygen Evolution Reaction in a Stable Bimetal-Organic Framework System. *Angew. Chem. Int. Ed.* **2018**, *57*, 9660–9664. [CrossRef]
46. Glomb, S.; Woschko, D.; Makhloufi, G.; Janiak, C. Metal-Organic Frameworks with Internal Urea-Functionalized Dicarboxylate Linkers for SO2 and NH3 Adsorption. *ACS Appl. Mater. Interfaces* **2017**, *9*, 37419–37434. [CrossRef] [PubMed]
47. Thommes, M.; Kaneko, K.; Neimark, A.V.; Olivier, J.P.; Rodriguez-Reinoso, F.; Rouquerol, J.; Sing, K.S.W. Physisorption of gases, with special reference to the evaluation of surface area and pore size distribution (IUPAC Technical Report). *Pure Appl. Chem.* **2015**, *87*, 1051–1069. [CrossRef]
48. Gurvich, L.G. Physico-chemical force of attraction. *J. Phys. Chem. Soc. Russ.* **1915**, *47*, 805–827.
49. *APEX2. Data Collection Program for the CCD Area-Detector System*, Version 2.1-0; Bruker Analytical X-ray Systems, Madison (WI), USA, **1997–2014**.
50. *SAINT. Data Reduction and Frame Integration Program for the CCD Area-Detector System*; Bruker Analytical X-ray Systems, Madison (WI) USA, 1997–2014.
51. Sheldrick, G.M. *SADABS: Area-Detector Absorption Correction*; University of Göttingen: Göttingen, Germany, 1996.
52. CrysAlisPro. *Rigaku Oxford Diffraction*; release 1.171.40.103a; Agilent Technologies UK Ltd.: Yarnton, UK, 2021.
53. Sheldrick, G.M. Crystal structure refinement with SHELXL. *Acta. Crystallogr. Sect. C Cryst. Struct. Commun.* **2015**, *C71*, 3–8. [CrossRef]
54. Sheldrick, G.M. A short history of SHELX. *Acta. Crystallogr. Sect. A Found. Crystallogr.* **2008**, *64*, 112–122. [CrossRef]
55. Dolomanov, O.V.; Bourhis, L.J.; Gildea, R.J.; Howard, J.A.K.; Puschmann, H. OLEX2: A complete structure solution, refinement and analysis program. *J. Appl. Crystallogr.* **2009**, *42*, 339–341. [CrossRef]
56. Brandenburg, K.; Putz, H. *Diamond, Crystal and Molecular Structure Visualization, Crystal Impact—Gbr*, Version 4.5; Bonn, Germany, **2009–2018**.
57. Turner, M.J.; McKinnon, J.J.; Jayatilaka, D.; Spackman, M.A. Visualisation and characterisation of voids in crystalline materials. *CrystEngComm* **2011**, *13*, 1804–1813. [CrossRef]
58. McKinnon, J.J.; Spackman, M.A.; Mitchell, A.S. Novel tools for visualizing and exploring intermolecular interactions in molecular crystals. *Acta Crystallogr. B* **2004**, *60*, 627–668. [CrossRef] [PubMed]